Geometrically non-linear bending of plates: Implications in curved building façades

Submitted to Construction and Building Materials

Geometrically non-linear bending of plates: implications in curved building façades

Andrea SPAGNOLI[a]*, Roberto BRIGHENTI[a], Marco BIANCOSPINO[b], Marco ROSSI[b], Riccardo RONCELLA[a]

[a] Department of Engineering and Architecture, University of Parma, Parco Area delle Scienze 181/A - 43124 Parma - Italy – e-mail: spagnoli@unipr.it

[b] GL&SS Consulting Engineers, 19 Britton Street, London EC1M 5NZ – UK

Abstract. Curved glazed façades of buildings are often realized by cold bending of flat plates. This paper is devoted to experimental tests under static loading on the geometrically non-linear anticlastic bending of aluminium plates, whose constituent material is used as a phantom material to mimic the elastic mechanical behaviour of glass. The 3D displacement field of the plates is reconstructed through the use of the DIC (Digital Image Correlation) technique and several numerical FE analyses are performed to simulate the experimental results. A critical value, corresponding to a configuration of the plate where a change in its curvature sign occurs, of the applied displacement at the plate corner is determined. The results are discussed in terms of critical applied displacement against the plate thickness for different plate sizes. It is shown that the critical displacements are almost independent on the plate size, but linearly depend on the plate thickness.

Keywords: Plates; Anticlasting bending; Cold bending; Geometrical non-linearity; Glass.

1. Introduction

In modern architecture, buildings of complex shapes are more and more frequently designed [1,2] thanks, among others, to the development of software applications that allow advanced 3D modeling. This software has accelerated the development of free-form design, otherwise known as fluid design, in which curved surfaces play an important role. The rapid development of modeling software has filled the initial gap between the design stage of the building and its construction phase.

The value of a building is often judged from its exterior appearance, typically from the façade. Commonly, a large portion of modern building façades is occupied by transparent parts made of glass (e.g. see Refs [3-5] for an account on recent research related to glass façade structures) . The use of deflected glass plates facilitates the creation of continuous and sinuous envelopes that guarantee a perfect combination of aesthetics, transparency and use of natural light [6-10]. The use of curved plates is quite common also in other applications, such as in technology (silos, fuselages, cars body, etc.), in nature (cell membranes, lipid vesicles, skin, natural armors, etc.), and so on. Façade construction represents a very promising sector for the application of curved panels, because of the practically limitless final shapes that can be obtained.

Considering that free-form design of building skins often involves curved surfaces, glass panels need to follow given forms and established prescriptions. Traditionally, the production process of glass panels takes place at elevated temperatures, that is, flat glass panels are heated over the weakening point and gradually bent [11]. After cooling, the finished plate can keep the new configuration without the need for restraining forces along the sides. The disadvantages of this technique, however, are numerous, including: (i) high cost required for modeling; (ii) high energy consumption; (iii) risk of optical distortion [12]; (iv) difficulty of transport for a finished panel; (v) long waiting periods.

For these reasons, a more convenient production technique at room temperature has been developed to obtain curvatures in glass panels, called *cold bending* [13-20]. This technique involves the deflection of glass panels at room temperature directly on site by attaching them to a support structure (frame).

Cold bending is an elastic and reversible procedure that simplifies the laying down and cutting costs in glass façade engineering. The number of constructions based on this technique is constantly increasing, and today it encompasses very different types of structures, such as skyscrapers, airports, areas fairs, museums and shopping centers.

The glass used for the construction of buildings typically derives from silicates and basic soda. The typical values of the most important physical-mechanical parameters of soda-lime glass and borosilicate glass are: Young modulus E = 63-77 GPa; Poisson ratio ν = 0.20-0.24; mass density ρ = 2250-2750 kg/m^3; thermal expansion coefficient α = 3.3-9×10^{-6} K^{-1}; resistance f_t = 45, 70 and 120 MPa for annealed [21], heat strengthened [22] and toughened [23] float glass, respectively; fracture toughness K_{IC} = 0.75 MPam$^{0.5}$.

For structural applications, glass is generally considered as a homogeneous isotropic material. At temperatures below the transition point (which is 530 °C for a glass derived from silicates), it is generally accepted that a linear elastic mechanical behavior can be assumed. The linear response is abruptly interrupted when the breaking point is reached due to the brittle nature of the material.

The first appearance of the cold bent glass took place in 2005 during the construction of the Town Hall of Alphen aan de Rijn in the Netherlands by architect Erick van Egeraat [16]. The project included numerous randomly curved glass strips arranged in a way to form an 'egg-shaped' façade. For this reason, quadrangular panels were curved on site. To adapt panels to the envelope geometry, one corner of each panel was bent out of the panel's plane up to a maximum displacement of 40 mm with panel size of 900 mm × 2000 mm, so that to generate the desired deformed configuration. The effects of the cold bend on the glass plates were not well known at that time, and this led to the beginning of in-depth research. The performed study [16] focused on fixed quadrangular plates anchored point-wise at the corners to create a double-curved façade. Given the complex geometry, the connections were made using silicone sealing elements to match the different angles of the panels and to exploit the flexibility of the rubber material.

Cold bending of glass panels features complex non-linear phenomena related to the variation of internal forces due to geometrical variation of equilibrium configurations of the panels [24-27]. The aim of the present paper is the numerical and experimental study of the geometrically non-linear behavior in thin plates under bending. This behavior occurs when second-order membrane actions arise due to compatibility with in-plane restraint under certain boundary conditions at the plate

corners. Some interesting problems related to geometrically non-linear behaviour of thin-walled structures can be found for instance in Refs [27, 28].

The relevant technical literature often deals with square plates constrained on three corners and subject to a transverse force applied in the free one. The trivial equilibrium configuration is characterized by anticlastic curvatures, so that the supported diagonal is convex (curvature oppose to the force direction) while the loaded diagonal is concave (curvature in the force direction). At a critical value of applied force (or, alternatively, of imposed displacement) the loaded diagonal increases further its concavity while the supported one becomes more rigid, tending to assume a straight configuration, see Fig. 1 taken from Ref. [26]. This phenomenon is associated with a bifurcation instability in the equilibrium configuration path with a more than linear increase of the corner reactions and of the applied force necessary to reach a given value of curvature. Furthermore, this critical condition is characterized by the manifestation of superficial ripples on the plate, which, in the application case of glass panels, tend to distort the light rays that impact the surface of the glaze.

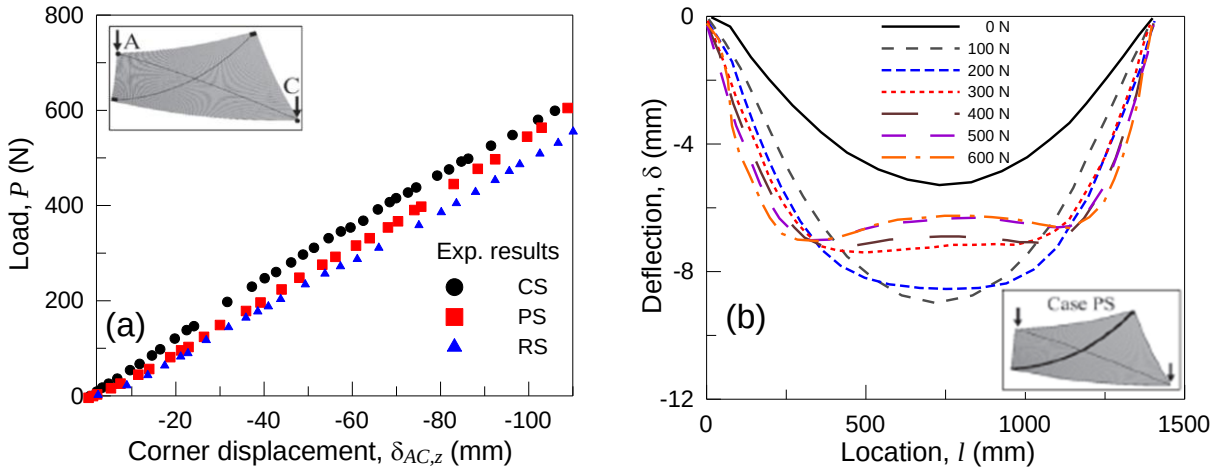

Fig. 1. (a) Experimental load-deflection curves (RS = roller support, CS = clamped support, PS = pin support); (b) Experimental deflection along pin supported diagonal, adapted from Ref. [26].

From the research of Ref. [17] it emerged that the critical condition of non-linear deflection of the plates does not depend on the characteristics of the material, but rather on the thickness of the plate and on its boundary conditions. In particular, the resulting critical displacement turns out to be linear dependent on the plate thickness.

This paper is devoted to perform experimental tests on aluminum plates; aluminum is used as a phantom material to mimic the elastic mechanical behaviour of glass because of the similar values

of the elastic constants in the two materials. Tests on square plates with dimensions 600×600 mm^2 and variable thicknesses of 1, 2 and 3 mm, constrained on three corners, were performed with constraints that prevent in-plane displacements but allow free rotations. A transverse displacement is imposed on one corner, up to a maximum value of 100 mm. The imposed displacement was applied with a screw connected in series to a load cell to measure the reaction force at the corner itself. The panels were treated with a white paint background and a random pattern of black dots made with a varnish spray. This treatment allows the use of the DIC (Digital Imagine Correlation) technique for a three-dimensional reconstruction of the displacements undergone by the plate, with respect to the undeformed reference configuration. In particular, the acquisition system of the images requires the use of two high-definition cameras. A specific software, allowing the full-field reconstruction of the field of displacements and deformations in the plates, has been used. The results of the experimental tests are presented in terms of out-of-plane displacement maps. These results are compared with those obtained by a FE modeling of the plates, focusing in particular on the displacement imposed in the free corner, on the mid-point curvature along the supported diagonal, on the central deflection of the plate and on the reaction force acting in the free corner. These trends show that the reaction force grows more than linearly with respect to the applied displacement, due to non-linear coupling effects between membrane and bending actions.

The most significant result concerns the trend of the curvature in the central point of the plate: initially convex, this curvature has an increasing trend until reaching a peak value beyond which it decreases and changes sign. The inflection point of the central curvature corresponds to the critical condition of instability, and the corresponding displacement applied in the free corner is defined as critical displacement. The obtained experimental and numerical results demonstrate a linear relation between critical displacement at the free corner and the plate thickness. This law is considered to offer useful guidelines in the practical application of realizations of curved glass panels through the use of the cold bending technique.

The paper is organized as follows: in Section 2 a brief overview on the anticlastic bending of plates is provided, while Section 3 illustrates the experimental campaign, the measuring technique adopted to reconstruct the full 3D displacement field of the bent plates and illustrates and discusses the obtained results. Section 4 is devoted to the FE numerical analysis of the problem, and, finally, Section 5 outlines some conclusions.

2. Anticlastic bending of plates

Let us consider a rectangular thin plate with free sides. The boundary conditions at the four corners can be either kinematic or static, i.e. prescribed displacements $w(x=0,a;y=0,b)=\delta_i$ where $i=A,B,C,D$, or $R_i=2m_{xy}(x=0,a;y=0,b)=F_i$ (see Fig. 2).

The linear Kirchhoff–Love plates theory [29,30] predicts that the deformed shape is a hyperbolic paraboloid, which preserves the straightness of the edges. The kinematic model of Kirchhoff causes concentrated forces at the plate corners, consequent of opposite twisting moments at the corners themselves; using plate theories accounting for shear deformation, such as Mindlin's theory [31,32], would yield non concentrated forces at the corners. The solution of Germain-Lagrange equation yields a bilinear function for the plate deflection, characterized by an anticlastic curvature (e.g. see Ref. [33]). The only internal non-zero action in the plate is the twisting moment m_{xy} which turns out to be constant. If the four corners are loaded by a set of self-equilibrated forces $R_A=R_B=R_C=R_D=F$ (see Fig. 2) the resulting deflection is as that shown in Fig. 3 and it is expressed by

$$w(x,y)=\frac{6F\left(1+\nu\right)}{Et^3}\left(x-\frac{a}{2}\right)\left(y-\frac{b}{2}\right)=\frac{\delta_D}{ab}\left(x-\frac{a}{2}\right)\left(y-\frac{b}{2}\right) \tag{1}$$

where $F=\dfrac{Et^3}{6\left(1+\nu\right)ab}\delta_D$. Note that the four sides of the plate remain straight. In the following, the plate is loaded by imposing a prescribed displacement at the corner D, δ_D, while the other corners are fixed, $\delta_A=\delta_B=\delta_C=0$. The resulting deflection (Fig. 3) is mathematically expressed through the bilinear relationship:

$$w(x,y)=\frac{\delta_D}{ab}xy \tag{2}$$

Note that the latter can be obtained from the deflection of Eq. 1 by superimposing a rigid translation along the z axis equal to $\delta_D/4$ and a rigid rotation about the diagonal AC. In other words, the anticlastic bending described by Eq. 1 is equivalent (in terms of displacement and stress/strain field) to that of Eq. 2, where three corners remain fixed and the transverse displacement is applied only to the fourth corner.

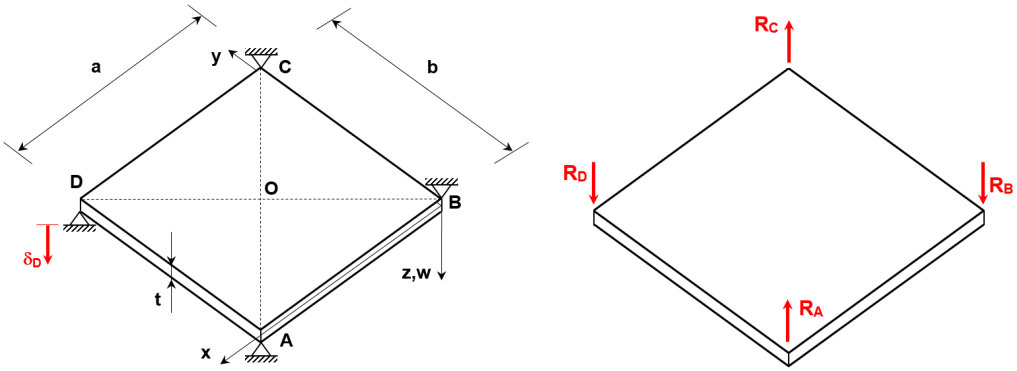

Fig. 2. Geometry of the plate and scheme of the corner forces.

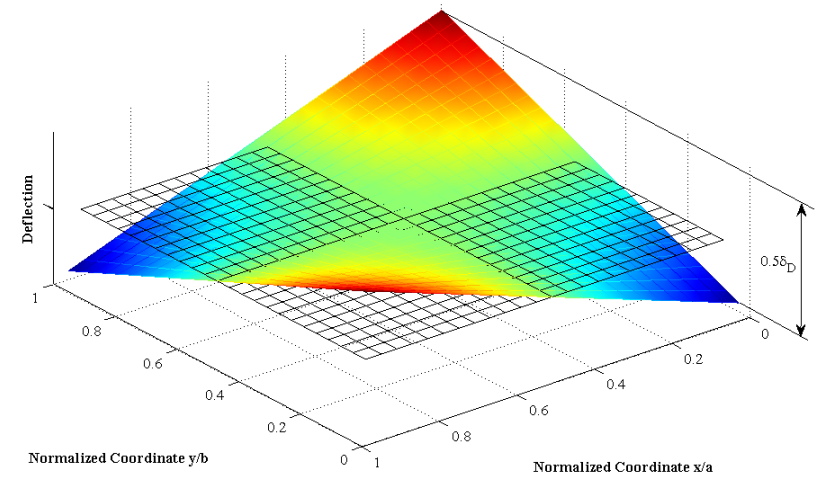

(a)

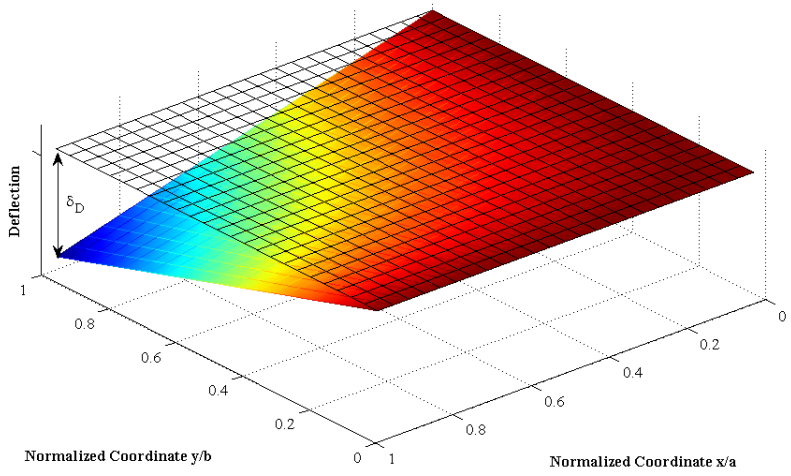

(b)

Fig. 3. Anticlastic deformation of the plate in the case of (a) self-equilibrated state; (b) prescribed displacement on a single corner.

According to the inextensional theory of Mansfield [34, 35], it is assumed that an initially flat inextensible surface can deform only into a developable surface, so that at each point there exists one straight line (generator) belonging entirely to the deflected surface. In other words, according to

the well-known Gauss' theorema egregium [36], the Gaussian curvature – defined as the product of the two main curvatures evaluated in a given point of the plate – cannot be changed without stretching the plate itself. If one considers for a square plate an inextensional deflection into a cylindrical surface, generators are given by straight lines parallel to the supported diagonal AC. For a square plate, the resulting load-deflection linear relation is [35]:

$$F = \frac{2}{(1-\nu)} \frac{Et^3}{6(1+\nu)a^2} \delta_D \tag{3}$$

By considering the geometric non-linearity of small strains but finite rotations, von Karman theory of elastic plates can be used. Galuppi et al [24] considered the total potential energy functional in von Karman theory; by assuming the bilinear deflection shape of Eq. (1) to approximate the out-of-plane displacement $w = w(x, y)$, a single degree of freedom system is obtained and the stationarity of the functional reduces to a simple algebraic minimization. Such a minimization is performed for each value of the force F, leading to a non-linear relation $F - \delta_D$. A less stiff, i.e. relaxed, solution is proposed in Ref. [24], by considering a 'double cylindrical' deflection obtained by two successive movements in two orthogonal directions.

3. Experimental study

3.1. Testing set up

Square plates of a = 600 mm in side made of aluminum are tested. Aluminum material is adopted as a substitutive of glass, thanks to its similar mechanical properties (e.g. see Ref. 37]). In particular, for aluminum E = 70 GPa, ν = 0.33 while glass attains typically values of E = 70 GPa and ν = 0.22. The difference in the Poisson ratio is deemed not to be relevant in affecting the experimental results. Three values of plate thickness t are considered, i.e. 1, 2 and 3 mm (a/t = 0.0016, 0.0033, 0.05).

With reference to the notation of Fig. 2, plates are supported by spherical hinges at three corners A, B and C, while in the fourth corner D a prescribed displacement δ_D is applied (Fig. 4). The constraints are created with rotation free small steel plates of size 30x30mm tightened with two screws and located on the two sides of the plate. The plates are slightly imprinted to be able to allow the tightening screw a greater grip and guarantee the rotation capacity of the constraint. A

hard rubber is also glued to improve the contact friction between sample plate surfaces and the constraining small steel plates.

Once the set-up for DIC technique is arranged (see Section 3.2 below), photographs of the plate are taken at each imposed transversal displacement at corner D with steps of 2.5 mm up to achieve the expected final displacement of 100 mm (40 in total). Note that the transversal displacement at corner D is actually imposed by means of a threaded rod whose axis is fixed while the plate deflects: this causes a slight movement along the plate surface of the point where the displacement is imposed. At each step, the reaction force R_D at the corner, where the displacement is prescribed, is recorded. Since tests are performed in the elastic range of the material, reproducibility of the tests is conducted by cyclic repetition of the imposed displacement.

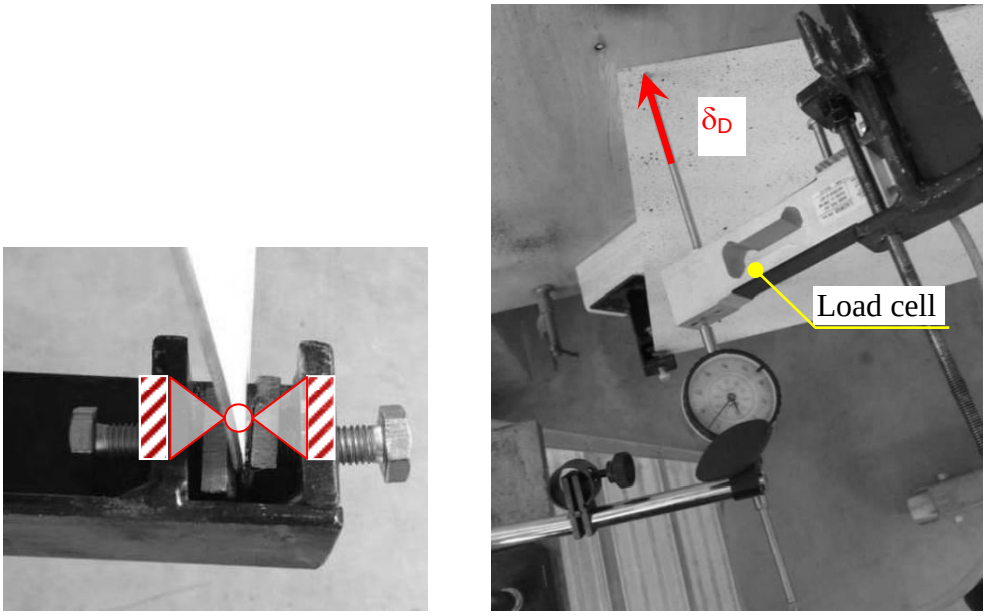

Fig. 4. Detail of the experimental boundary condition at the corners (see corners A, B and C in Fig. 2). Detail of the applied displacement at corner D.

3.2. 3D Digital image correlation technique

3.2.1. Photogrammetric Setup

The photogrammetric setup to evaluate the full field displacement/deformation of the plates under loading, requires accuracy in surface point 3D positioning and robustness of plate surface reconstruction.

Full-format Nikon D3X (resolution: 6048×4032 pixels) and Nikon D800 (resolution: 7360x4912 pixels) DSLR (Digital Single-Lens Reflex) cameras are used to image the specimen during the test from fixed positions, about 3 meters far from the plate, with a base-length of approximately 2 m in a convergent configuration (about 30°). The D3X camera is equipped with a FX CMOS sensor and assembled with a 105 mm Sigma optics which produced a pixel size on the object (Ground Sampling Distance – GSD) in the range 0.165-0.175 mm. The Nikon D800 camera is equipped with a FX CMOS sensor with similar signal to noise ratio but with a higher resolution (36 Mpixel vs 24 Mpixel). Using a fixed 90 mm focal length f/2.8 Tamron optics the resulting GSD is in the range 0.158-0.168 mm, that is, the ground resolution of the two cameras are basically the same during the tests. With such imaging geometry, the *a priori* precision along the direction orthogonal to the plate surface (i.e. along which out-of-plane displacements occur) is estimated [38] in about 0.13 mm.

Interior and distortion camera parameters estimation, as well as Ground Control, are not considered critical for the experiments since only relative displacements orthogonal to the plate are required. Small amount of unaccounted 3D model deformations of the photogrammetric reconstructed plate surface due to systematic errors, e.g. due to inaccuracy in imaging geometry or camera model, are the same for all the stereo-pairs taken under loading and eliminated during the comparison with the baseline pairs. Nonetheless, a strongly redundant self-calibration setup is employed for both cameras, in order to limit such effects. Fixing the camera focus, 20 images for both the D3X and D800 were acquired with a strongly convergent imaging geometry, framing the plate and its surrounding. Subsequently, using more than 7400 tie points automatically extracted on all the images, using a Least Square fitting algorithm implemented in the CALGE bundle adjustment routine [39], the parameters of the Brown model [40] are estimated. The results, after LS adjustment, show low residuals (approx. 0.6 pixel RMSE for image observations), good a-posteriori precisions for all the Brown model parameters (e.g. focal length is equal to 3 μm) and low correlations between the parameters themselves, except between the radial distortion parameters, which is quite common with long focal length optics. The maximum image distortion is limited: 8 pixels for the Nikon D800/Tamron camera and 18 pixels for the NikonD3X/Sigma camera in image corners.

The four points at the corners of the plate are considered as Ground Control Point (GCP), as they are supposed to lay on the same plane (i.e. the Z coordinate of the four points is assumed to be null). Although some residuals of about 1 mm after bundle adjustment indicate that the plate is not perfectly planar at the beginning of the loading test, the coordinate reference XY plane represents a good approximation of the mean planar surface of the plate specimen.

3.2.2. Image processing and displacement field estimation

Image acquisition is performed by the cameras at each load step through a synchronous acquisition of a single full-resolution frame. The cameras are remotely controlled, in order to guarantee their position and pose during the test, and consequently maintaining the reference system fixed.

The plate specimens were previously painted before testing with a random pattern of small, size and shape varying, dots, providing a full-field set of features that can be tracked (evaluating their 3D position) during the experiments (Fig. 5). Comparing these features, obtained from the two cameras at the same loading instant, with image matching algorithm allows reconstructing the 3D digital model (or Digital Surface Model – DSM) of the deformed plate. The out-of-plane displacements of the plate in the Z direction (i.e. normal to the undeformed plate) can easily be computed comparing DSMs at different loading instants (see Figs 6 and 7). On the contrary, tracking corresponding points on the images at different instant allows evaluating in-plane displacements/deformations. In the present experimental campaign, the latter measurements are not considered since in-plane displacements are deemed to be as small as the photogrammetric precision of the present experimental set-up.

Two different matching algorithms are used and compared to obtain the final results: the first uses a Least Squares Matching local (i.e. every image point are considered individually and its final correspondent point is evaluated regardless of the neighbor matches) approach [41,42], while the second implements a Semi-Global Matching (SGM) algorithm [43]. The latter performs a pixel-wise matching, simultaneously considering all the possible matching solutions for all the points of the plate and accounting concurrently image similarity and displacement continuity. More precisely, it realizes the minimization of a global cost function, where matching scores of each single image point of the image (function of the reciprocal position of corresponding points on the two images and accounting both the image similarity and the regularity of the displacement field) are summed. To find the optimal matching solution (i.e. the one that minimizes the global cost function), considered the high dimension of the solution space, the implemented algorithm [44] uses a Dynamic Programming (DP) approach. For sub-pixel estimation of the final disparity solution, the position of the minimum is usually calculated by fitting a quadratic curve through the cost values of neighboring pixels.

At the end of the matching stage, the 3D positions of corresponding points are computed using forward intersection: with both LSM and SGM, every single pixel position is considered. The resulting point cloud consists of more than 4.2 million of 3D points. Finally, in order to reduce the noise of the matched data and make the subsequent comparison and analysis more efficient and less prone to isolated outlier, the point cloud is interpolated on a regular grid (600 × 600 elements, i.e. one sample per mm on the plate surface) fitting the surface with a 4^{th} order complete polynomial function.

The comparison of the results (i.e. the DSM of the plate at each measurement step) obtained using LSM and SGM shows that the two approaches achieve similar displacement fields. The RMS of the differences between the two point clouds (before the polynomial fitting) are generally lower than three times the expected precision (i.e. about 0.04 mm). However, the regularization term implemented in the SGM approach results in smoother surfaces, while the LSM, especially in some plate areas, where the painted pattern shows less contrasted features, tends to produce some outliers. For this reason, in the subsequent analysis, only the results obtained with the latter approach (SGM) are considered.

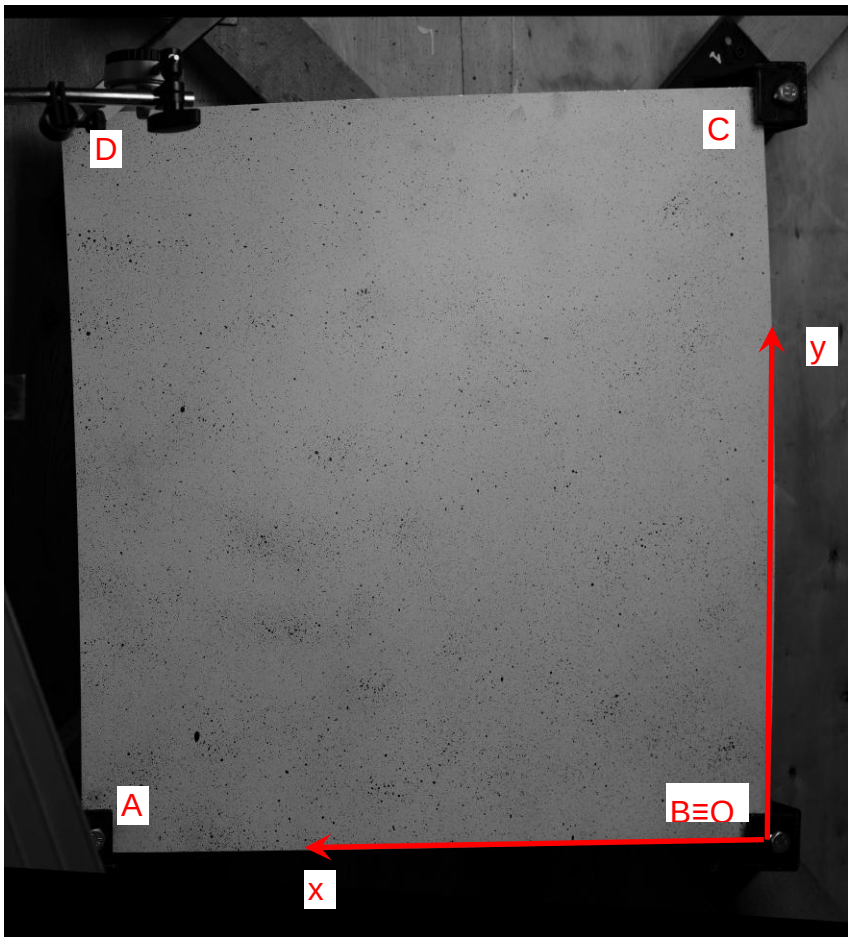

Fig. 5. Front view of the plate specimen, with the spray painted pattern in black & white for DIC technique application.

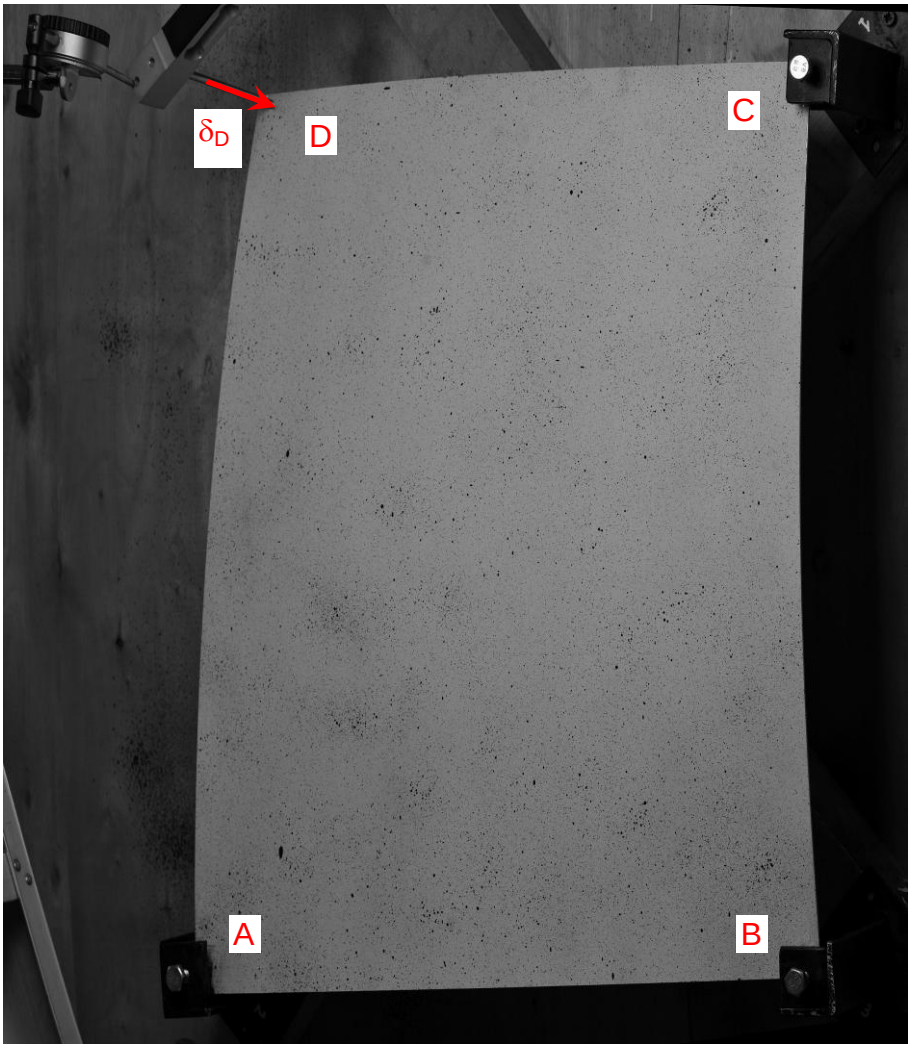

Fig. 6. Front view of the plate specimen, under prescribed displacement at corner D.

Fig. 7. Side view of the plate specimen, under prescribed displacement of 100 mm at corner D: the significant deflection can be appreciated.

3.3. Results

The experimental deflection of the plate specimens obtained with DIC are fitted with a 4^{th} order complete polynomial expression. The 3D plot is shown in Fig. 8 at two levels of applied displacement at corner D. Note that the deflection is represented for the whole 600 × 600 mm^2 domain of the plate, but it should be borne in mind that constraints are located at a distance from the corners so that the centroid-to-centroid distance of supports is about 570 mm (effective size of the plate).

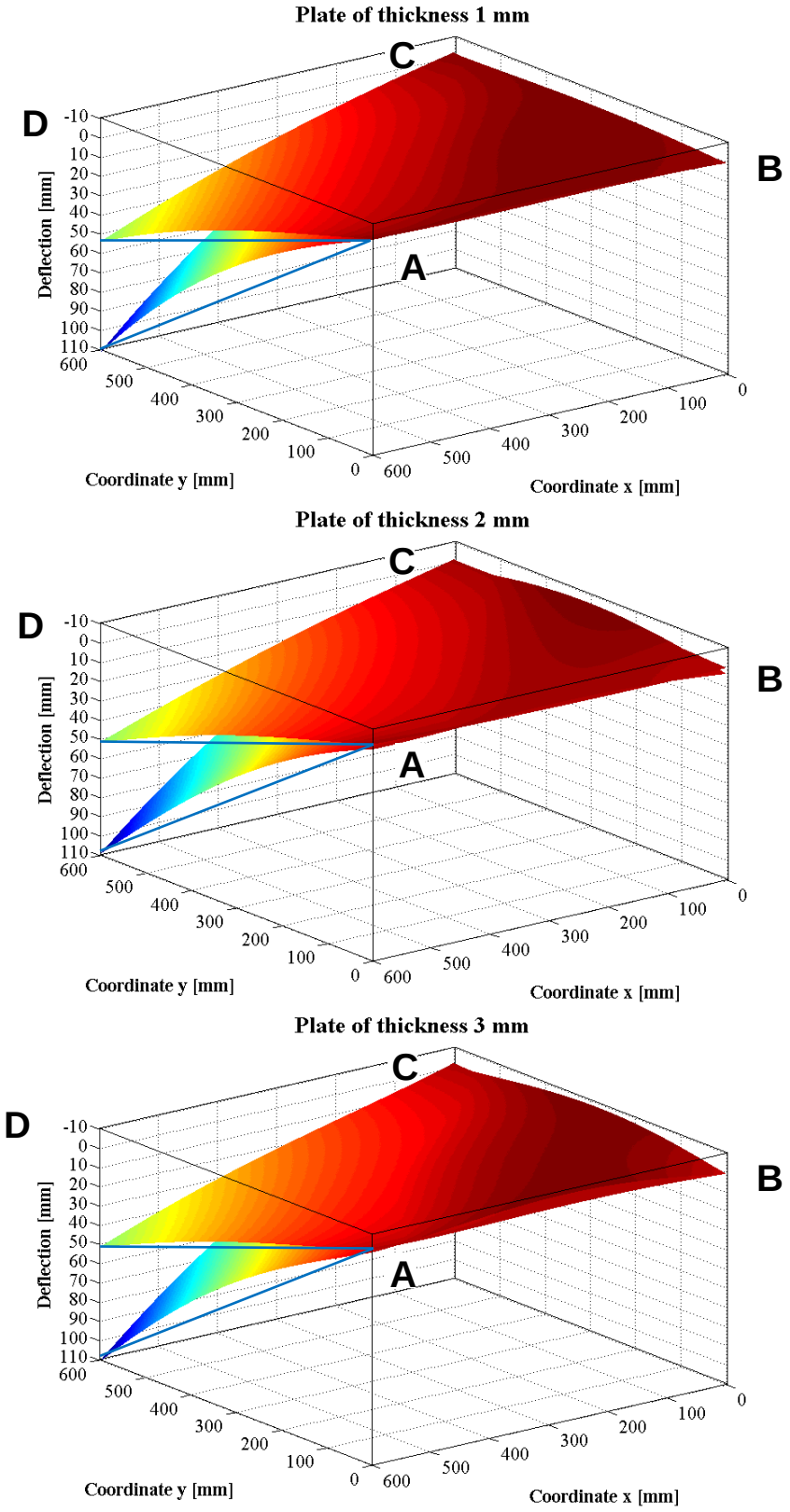

Fig. 8. 3D plot with contour map of the experimental deflections in the plates of different thickness, under prescribed displacement at corner D equal to about 50 mm and 100 mm. In the plots, blue lines are reported to visually appreciate the curvature under loading of the initially straight edge AC of the plate.

The out-of-plane deflections, measured along the supported diagonal AC (left column of Fig. 9) and the loaded diagonal BD (right column of Fig. 9) obtained from experiments at different levels of applied displacement at corner D, are shown in Fig. 9.

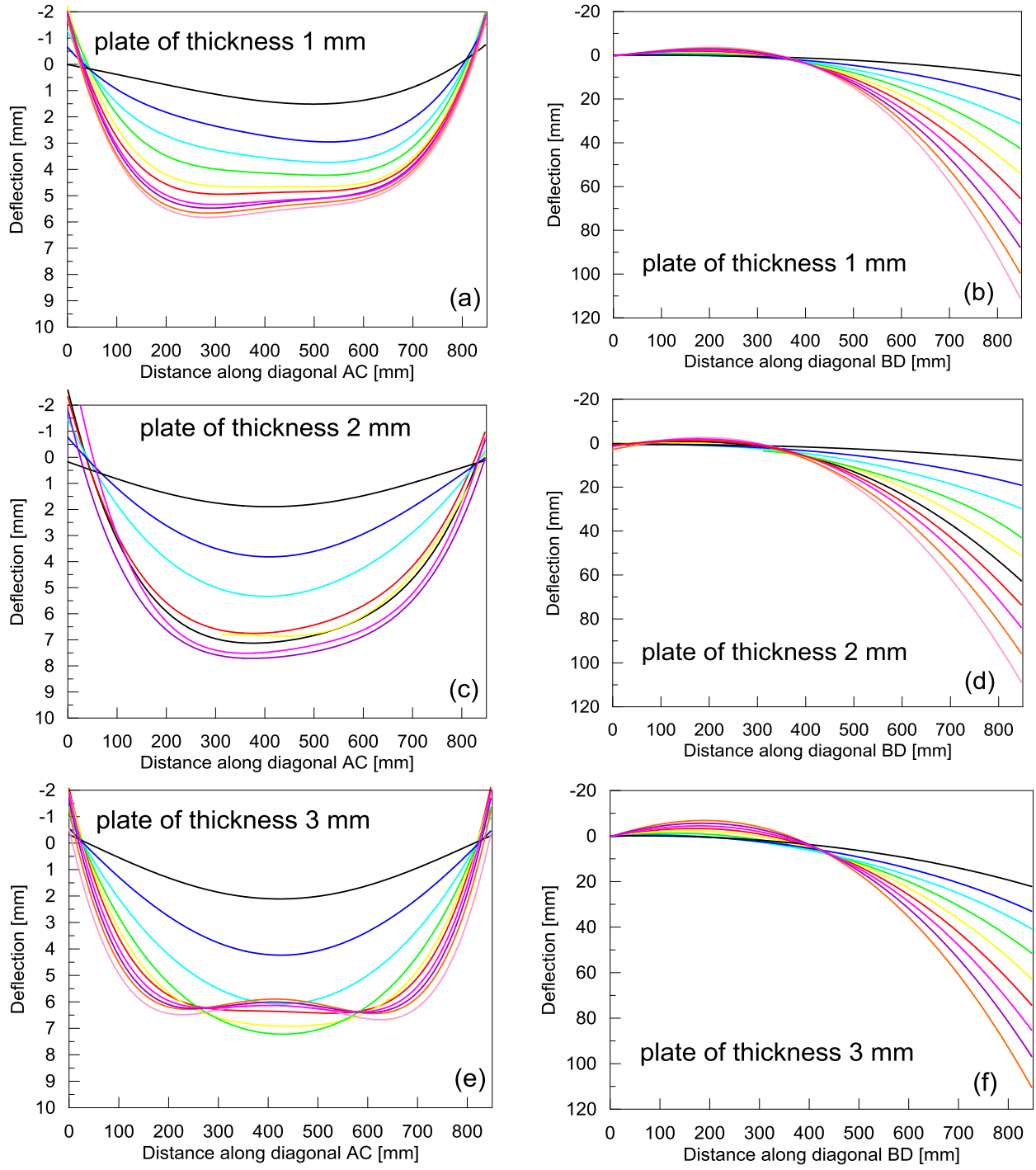

Fig. 9. Experimental deflection of the plate with different thickness along the two diagonals. Deflection profiles are reported in different colours at step of 10 mm in the applied displacement at corner D (the curves in (c) related to the two final steps of displacement application are disregarded due to some measurement errors).

It can clearly be observed that along the supported diagonal, a change of sign in the curvature occurs at a certain level of the applied displacement at corner D, while curvature along the loaded diagonal continuously increases with applied displacement. It can be noticed that, due to the adopted 4th order polynomial fitting of the results and to the effective distance between supports in the plate specimens, some deflections are negative along the supported diagonals near the corners (the same trend of results is expected if higher order polynomia were adopted).

4. Numerical simulation

The numerical analyses are performed using a 3D mesh with solid 20-node quadratic brick elements with reduced integration (referred to as C3D20R in the ABAQUS library [45]). Four elements are used along the thickness, and the number of elements in the mean plane of the plate is 57 × 57, so that each element is 10 mm in size (the plate size of the FE model is based on the distance between the supports in the experimental set-up), see Fig. 10. The maximum aspect ratio is equal to unity on the XY plane. The mesh adopted is obtained after a convergence study and it is in line with previous investigations [24].

The FE model of the plate is constrained at the corner by assuming zero displacements along x, y and z direction at the central node along the thickness at corners A, B and C. At corner D, the displacement along the z direction of the central node is prescribed, being the displacements along x and y free (see Fig. 11).

A geometrically non-linear FE analysis using an updated Lagrangian approach is performed. Accordingly, current nodal coordinates are updated at each step by adding the solution displacements in the step to the coordinates in the original configurations. Strain are assumed to be small and the material is linear elastic and isotropic (E = 70 GPa, ν = 0.33).

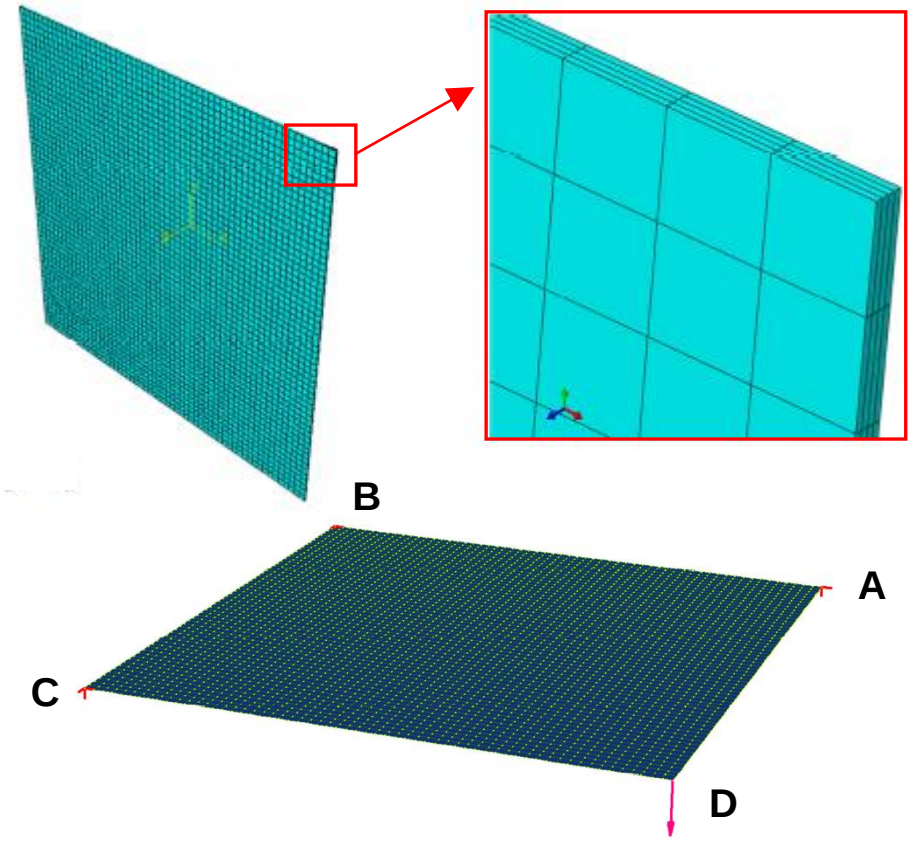

Fig. 10. Adopted FE mesh of the plate.

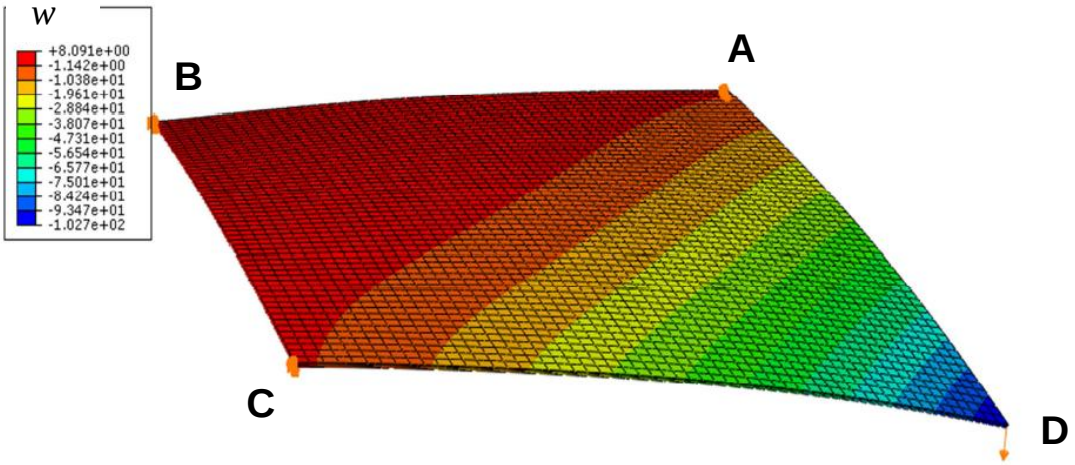

Fig. 11. Out-of-plane deflection of the plate with contour of the out-of-plane displacement w along the Z axis (mm) when the corner D is displaced by 100 mm.

4.1. Comparison with experimental results

A comparison between FE results and experimental findings is carried out with reference to the curves of force vs prescribed displacement $R_D - \delta_D$, mid-point deflection vs prescribed displacement $\delta_O - \delta_D$ and mid-point principal curvature vs prescribed displacement $\chi_O - \delta_D$. For the $R_D - \delta_D$ curve a comparison is also made with respect to the theoretical linear results of Kirchhoff [30,31] and of Mansfield [34,35].

In the FE analysis, the curvature is calculated in the middle of the plate along the supported diagonal using a local reference system. For each load step, the difference between the deformation along the supported diagonal on the bottom part of the plate (i.e. at $z = t/2$) and the corresponding deformation on the top part of the plate (i.e. at $z = -t/2$) at the plate centre is considered (nodal values of strains are extrapolated from those evaluated at the Gauss points of the elements). By dividing this difference by the thickness of the plate, the principal curvature value, χ_O, can be calculated, namely

$$\chi_0 = \frac{\varepsilon_{\text{inf}} - \varepsilon_{\text{sup}}}{t} \tag{4}$$

The curvature in the experimental study is calculated through the finite difference method. All the fitted data from the DIC technique are elaborated in order to consider the out-of-plane sampled displacements along the supported diagonal. In particular, by considering the point *i* at plate centre and the two near points along the supported diagonal, we have

$$\chi_0 = \frac{w_{\text{i+1}} - 2w_{\text{i}} + w_{\text{i-1}}}{h^2} \tag{5}$$

where *h* is the sample spacing of the experimental points along the diagonal.

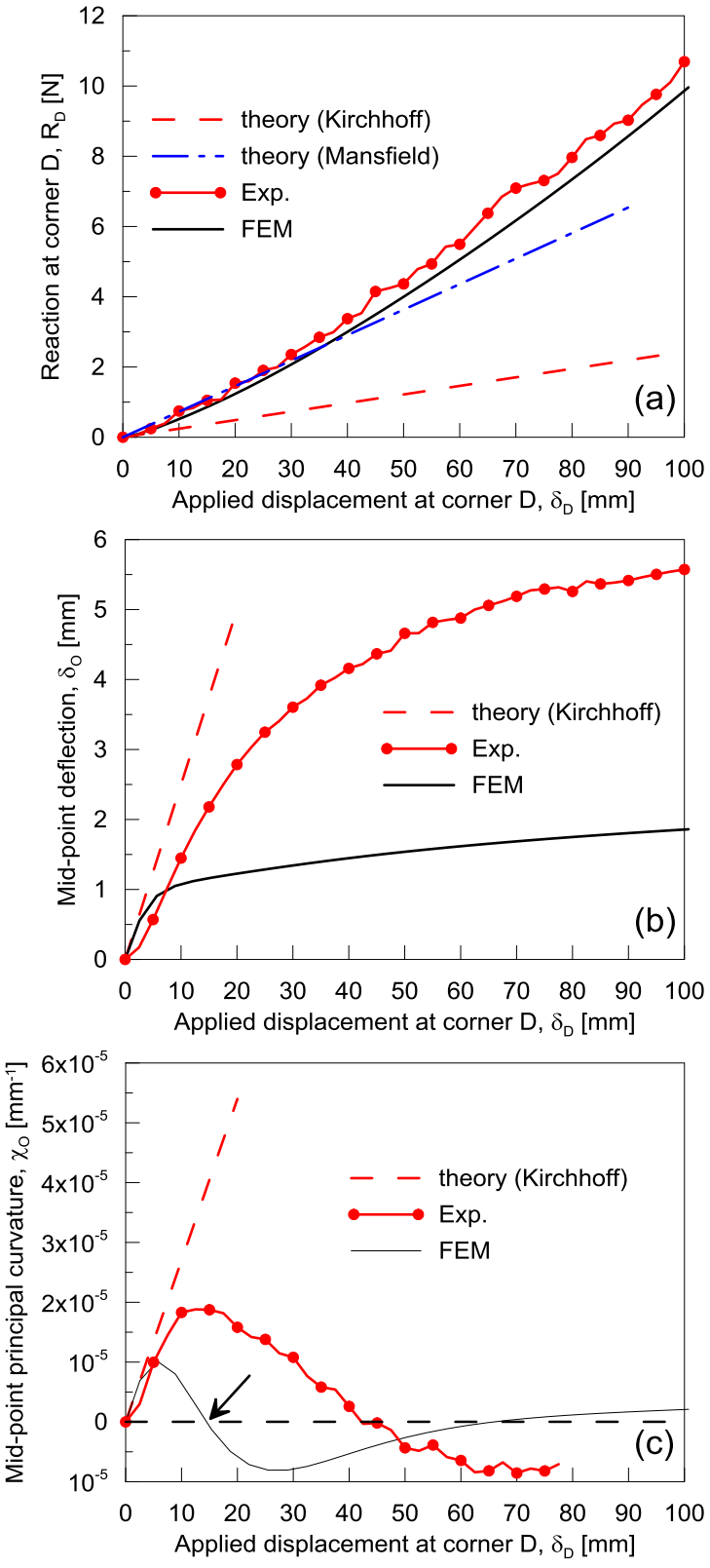

Fig. 12. Comparison of experimental results with FE and theory, plate with thickness 1 mm.

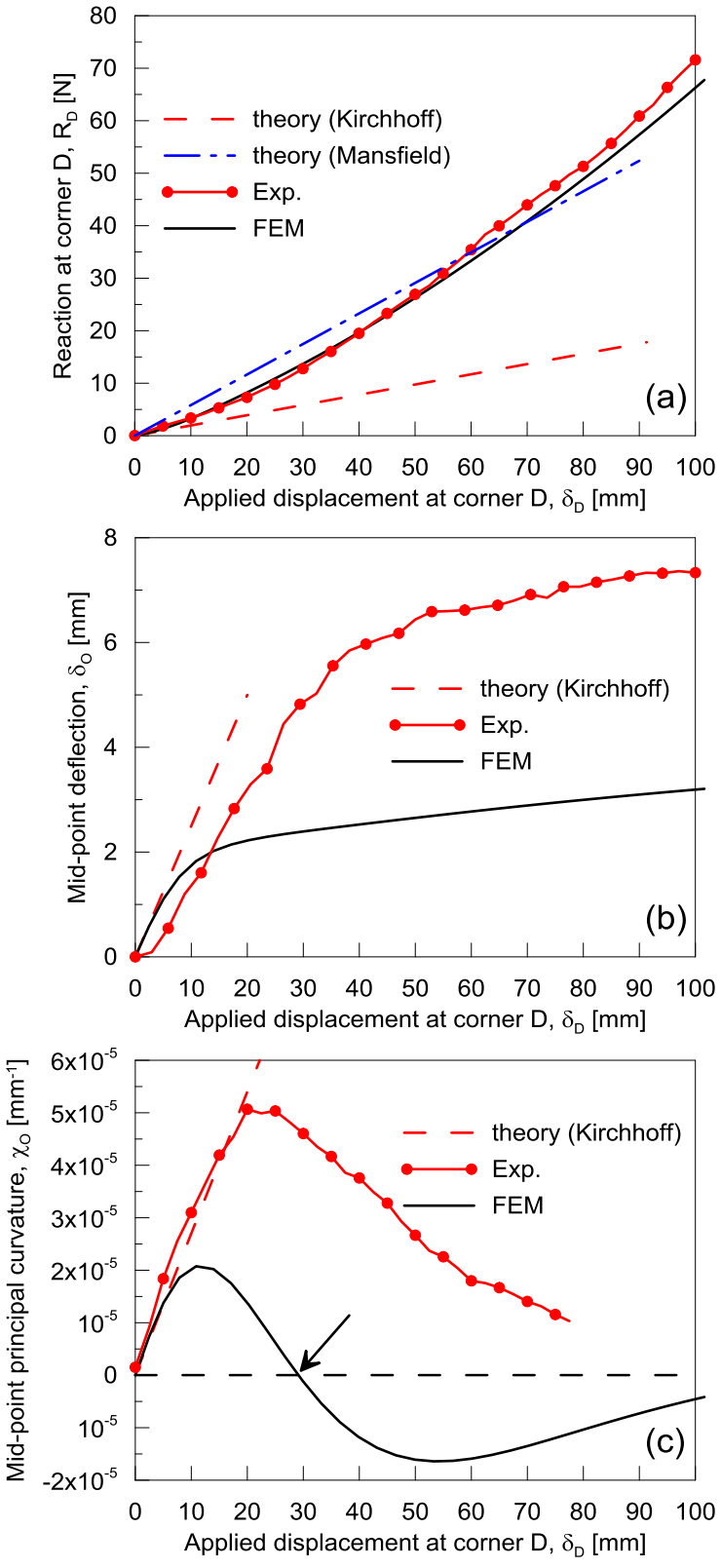

Fig. 13. Comparison of experimental results with FE and theory, plate with thickness 2 mm.

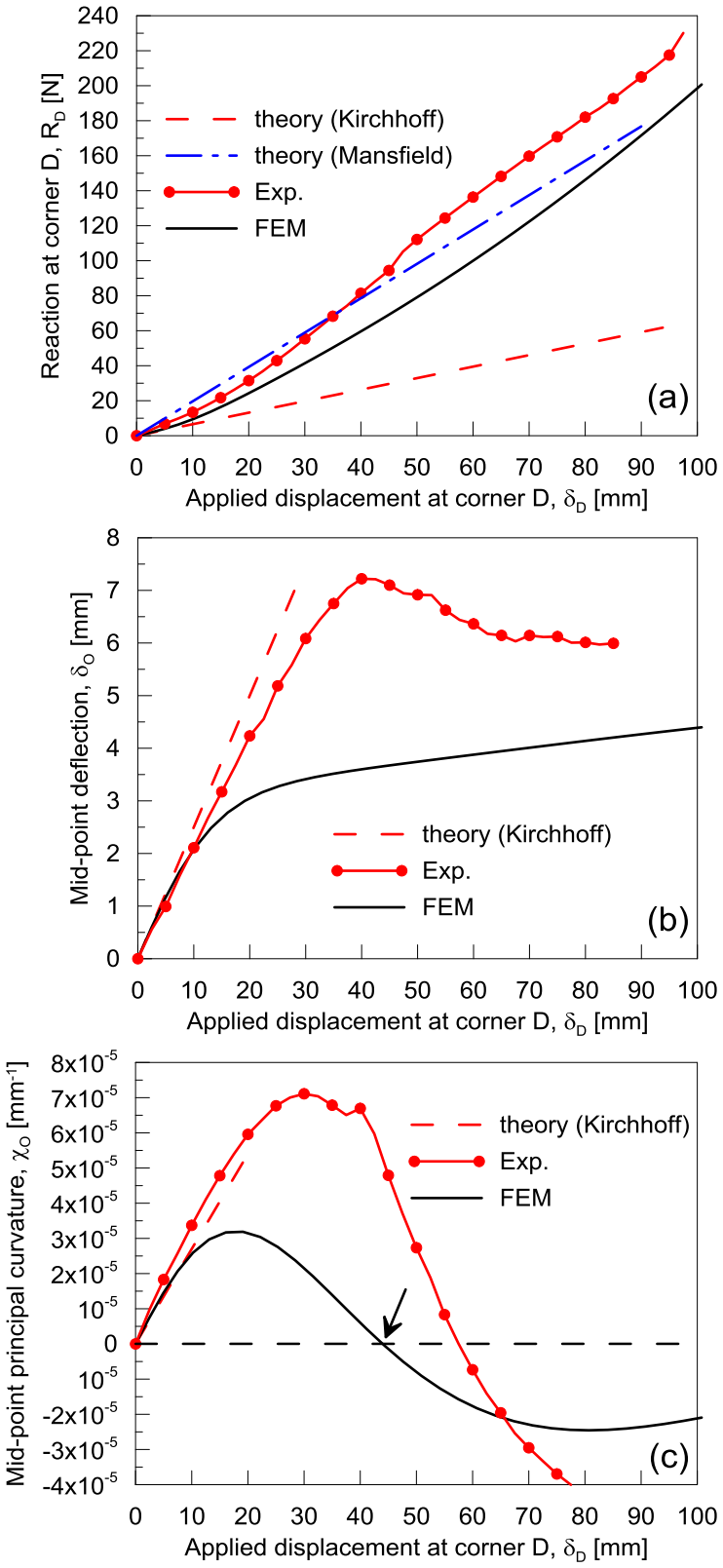

Fig. 14. Comparison of experimental results with FE and theory, plate with thickness 3 mm.

The results in terms of maximum principal curvature against applied displacement (Figs. 12(c), 13(c) and 14(c)) illustrates the geometrically non-linear phenomenon associated with an initial

increase of the curvature along the supported diagonal AC up to a maximum. Beyond a certain value of the applied displacement, such a curvature starts decreasing followed by a change of sign. The value of the applied displacement at corner D at which the curvature is null is regarded as the critical displacement $\delta_{D,cr}$ (see arrows in Figs. 12(c), 13(c) and 14(c)).

The overall comparison between experiments and FE model is quite satisfactory in the initial stage of the plate deflection (Figs. 12-14), particularly for the case of plate thickness 3 mm. The comparison with linear results shows that the non-linear phenomena under investigation lead to a progressive increase of the stiffness from the initial value of Kirchhoff theory to that of Mansfield theory (see Figs. 12(a), 13(a) and 14(a)).

4.2. Parametric study

The FE analyses are extended to different sizes of square plates, ranging from 300, 600 up to 1200 mm. The plate thickness is varied between 1 and 6 mm. Eighteen different geometric combinations are analysed in this parametric study with the aim of exploring the influence of plate geometry on the applied critical displacement, $\delta_{D,cr}$, where such a displacement is defined with the criterion of zero principal curvature at mid-point of the supported diagonal. The mechanical properties and boundary conditions are kept the same as those used in the FE model for experimental comparison.

The results in terms of applied critical displacement against the plate thickness are shown in Fig. 15 for different plate sizes. It is shown that the results are almost independent on the plate size, while the trend is approximately linear with slope of about 14.75, that is $\delta_{D,cr} = 14.75t$.

As mentioned above, $\delta_{D,cr}$ is dependent on the plate thickness, but not on its size. If one considers the critical event in terms of the overall curvature $\chi = 1/\rho$ of the plate induced by the applied displacement, a dependence on the plate size turns out. As a matter of fact, considering an overall cylindrical deflected shape of the plate due to the applied displacement δ_D we can write

$$\delta_D = \rho(1-\cos\vartheta), \quad \rho\vartheta = a \tag{6}$$

where ϑ is the central angle subtended by the cylindrical deflection. The resulting curvature is approximately equal to $1/\rho = 2\delta_D / a^2$, meaning that for plates of the same thickness the critical overall curvature decreases with the square of the plate side.

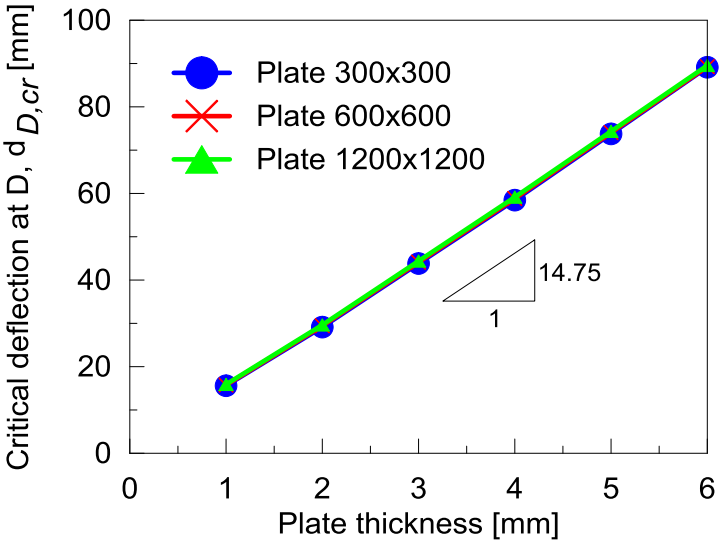

Fig. 15. Applied critical displacement against plate thickness for different plate sizes.

5. Discussion and concluding remarks

In the present paper, the geometrically non-linear problem of the anticlastic bending of plates is investigated, with reference to the application of cold bending of laminated glass panels used for instance in curved building façades. The study presents a detailed experimental campaign on aluminum plates which are deemed to mimic the mechanical behaviour of glass counterparts. In the experimental tests, full field displacement maps, obtained by means of a 3D DIC technique, allows us to capture the complex non-linear bifurcation behaviour of the plate exposed to increasing corner displacements. A change of sign in the plate central curvature along the supported diagonal is adopted as a criterion for identifying the critical value of the applied corner displacement $\delta_{D,cr}$. The experimental results are satisfactory described by detailed 3D FE models in terms of reaction corner force against applied displacement as well as of central curvature as well as applied displacement.

It is instructive to observe that in the paper of Staaks [17] a lattice model is conceived to describe the buckling phenomenon where the anticlastic configuration develops into an asymmetric one with one diagonal straightening and the other increasing curvature. The lattice model is composed by two diagonals acting as compressive struts while the four sides of the plate are tensile ties. The

elements are hinged one each other, and buckling occurs when the struts attain the critical condition of Euler flexural instability. According to this simple model, the resulting critical displacement turns out to be linear dependent on the plate thickness, and in the case of a square plate the critical displacement can be expressed as $\delta_{D,cr} = 3.35t$.

The same linear trend between the critical displacement and the plate thickness is observed in the present study. In particular the parametric study conducted on a number of FE models of plates with varying thickness and size shows a coefficient in the linear $\delta_{D,cr} - t$ relationship of 14.75, which is about four times larger than that of Staaks. This difference might be attributed to the fact that, oppositely to the assumption of the Staaks' model, the supported diagonal AC is found to be under tensile loading (clearly, due to the inflection along the diagonal, the distance between its two ends would reduce, but, because of the fixed distance between the two supports A and C, tensile forces develop for compatibility reasons). Such a tensile membrane stress tends to stiffen the plate deflection and in turn to increase the critical displacement for a given plate thickness. However, further investigation is needed to confirm the present conjecture and to develop simple mechanical models able to capture the key aspects of the phenomenon.

References

[1] Pottmann, H., Bo, P., Schiftner, A., Schmiedhofer, H., Baldassini, N., Wallner, J. Architectural freeform structures from single curved panels (2008) ACM Trans Graphics, 27 (3).

[2] Eigensatz, M., Kilian, M., Schiftner, A., Mitra, N.J., Pottmann, H., Pauly, M. Paneling architectural freeform surfaces (2010) ACM Transactions on Graphics, 29 (4), art. no. 45.

[3] Yu Wang, Qingsong Wang, Jinhua Sun, Linghui He, K.M. Liew, Effects of fixing point positions on thermal response of four point-supported glass façades, Construction and Building Materials, Volume 73, 2014, Pages 235-246.

[4] K. Martens, R. Caspeele, J. Belis, Membrane action in reinforced glass beam systems: Experimental setup and results, Construction and Building Materials, Volume 192, 2018, Pages 301-316.

[5] Chiara Bedon, Xihong Zhang, Filipe Santos, Dániel Honfi, Marcin Kozłowski, Michel Arrigoni, Lucia Figuli, David Lange, Performance of structural glass facades under extreme loads – Design methods, existing research, current issues and trends, Construction and Building Materials, Volume 163, 2018, Pages 921-937.

[6] Eekhout, M. and Niderehe, S. (2009). The new, cold bent glass roof of the Victoria & Albert Museum, London. Proc glass performance days, Finland, 408–412

[7] de Vericourt R. Inextensional theory applied to cold bent glass built-in stress evaluation. GPD 2011 Proceedings. 2011:377-83.

[8] Fildhuth T, Knippers J. Double curved glass shells from cold bent glass laminates. Proc glass performance days, Finland. 2011 Jun:384-9.

[9] Kassnel-Henneberg B. Purely structural glass building envelopes. Glass Performance Days. 2011 Jun:304-10.

[10] Raynaud, J. Resolution of the "Louis Vuitton pour la Création" glazed canopies technical challenge (2013) Proceedings of Glass Performance Days, p. 488.

[11] Saksala M. Curved and tempered glass–demand, challenge and opportunity for the market driven technology. Proc glass performance days, Finland. 2003:63-5.

[12] Abbott M, Madocks J. Roller Wave Distortion-Definition, Causes and a Novel Approach to Accurate, On-line Measurement. Glass Processing Days Proceedings. 2001 Jun:18-21.

[13] Vollers, K. and Veer, F. (2003). Usage of cold bent glass panes as an approximation for double curved surfaces. Proc glass processing days, Finland, 173–175

[14] Vákár, L.I. and Gaal, M. (2004). Cold bendable, laminated glass - New possibilities in design. Structural Engineering International: Journal of the International Association for Bridge and Structural Engineering (IABSE), 14, 95–97

[15] Eekhout M. Design, Engineering, Production & Realisation of Glass Structures for "Free-Form" Architecture. InCWCT members meeting. Bath, United Kingdom 2004.

[16] Eekhout M, Staaks D. Cold deformation of glass. In Proceedings International Symposium on the Application of Architectural Glass 2004.

[17] Van Herwijnen, F., Staaks, D., Eekhout, M. Cold bent glass sheets in façade structures (2004) Structural Engineering International: Journal of the International Association for Bridge and Structural Engineering (IABSE), 14 (2), pp. 98-103.

[18] Saksala, M. (2005). Extraordinary shapes with ordinary costs. Proc glass performance days, Finland, 371–373

[19] Belis, J., Inghelbrecht, B., Van Impe, R. and Callewaert, D. (2007). Cold bending of laminated glass panels. *Heron*, **52,** 123–146

[20] Neugebauer, J. (2014). Applications for curved glass in buildings. *J Façade Design Eng (JDFE)*, **2,** 67–83

[21] CEN - EN 572-2 Glass in building - Basic soda lime silicate glass products - Part 2: Float glass

[22] EN 1863-2:2004 Glass in building - Heat strengthened soda lime silicate glass - Part 2: Evaluation of conformity/Product standard

[23] EN 12150-2:2004 Glass in building - Thermally toughened soda lime silicate safety glass - Part 2: Evaluation of conformity/Product standard

[24] Galuppi, L., Massimiani, S., & Royer-Carfagni, G. (2014). Buckling phenomena in double curved cold-bent glass. International Journal of Non-Linear Mechanics, 64, 70-84.

[25] Galuppi, Laura, and Gianni Royer-Carfagni. "Optimal cold bending of laminated glass." International Journal of Solids and Structures 67 (2015): 231-243.

[26] Datsiou, K. C., & Overend, M. (2016). The mechanical response of cold bent monolithic glass plates during the bending process. Engineering Structures, 117, 575-590.

[27] P.W. Kneen, Prestressed membrane structures — The ultimate thin-walled structure, Thin-Walled Structures, Volume 9, Issues 1–4, 1990, Pages 135-149.

[28] Jianhui Hu, Yue Yin, Wujun Chen, Bing Zhao, Deqing Yang, Nonlinear structural behavior of flat-patterning ETFE cushion structures: Experimental observations and numerical simulations, Thin-Walled Structures, Volume 114, 2017, Pages 107-115.

[29] Kirchhoff, G. 4. Über das Gleichgewicht und die Bewegung einer elastischen Scheibe (1850) Journal fur die Reine und Angewandte Mathematik, 1850 (40), pp. 51-88.

[30] Timoshenko, S., Woinowsky-Krieger, S. (1959) Theory of Plates and Shells.

[31] Reissner, E. The effect of transverse shear deformation on the bending of elastic plates (1945) J. Appl. Mech., 12 (2), pp. A69-A77.

[32] Mindlin, R.D. Influence of rotatory inertia and shear on flexural motions of isotropic, elastic plates (1951) J. Appl. Mech., 18 (1), pp. 31-38.

[33] Gigliotti, M., Minervino, M. (2014) "The deformed shape of isotropic and orthotropic plates subjected to bending moments distributed along the edges", Meccanica, 49: 1367–1384.

[34] Mansfield, E.H. The inextensional theory for thin flat plates (1955) Quarterly Journal of Mechanics and Applied Mathematics, 8 (3), pp. 338-352.

[35] Mansfield EH. The bending and stretching of plates. Cambridge University Press; 2005 Aug 22.

[36] Pressley, A. (2010). Gauss' Theorema Egregium. In Elementary Differential Geometry (pp. 247-268). Springer, London.

[37] Datsiou, K. G., & Overend, M. (2014). Behaviour of cold bent glass plates during the shaping process. In *Engineered Transparency conference* (pp. 125-133).

[38] Fraser, C.S. (1996). Network Design. In K.B. Atkinson, editor, *Close Range Photogrammetry and Machine Vision*, chapter 9, pages 256-281. Whittles Publishing, Roseleigh House, Latheronwheel, Caithness, KW5 6DW, Scotland, UK

[39] Forlani, G. (1986) Sperimentazione del nuovo programma CALGE dell ITM. In: *Bollettino SIFET*, pp 63-72 (in Italian)

[40] Fryer, J. G., & Brown, D. C. (1986). Lens distortion for close-range photogrammetry. *Photogrammetric engineering and remote sensing*, *52*(1), 51-58.

[41] Gruen, A. (1985). Adaptive least squares correlation: a powerful image matching technique. South African Journal of Photogrammetry, Remote Sensing and Cartography, 14(3), 175-187.

[42] Ferrero, A.M., Migliazza, M., Roncella, R., Tebaldi, G. (2008) Analysis of the failure mechanisms of a weak rock through photogrammetrical measurements by 2D and 3D visions, Engineering Fracture Mechanics 75 (2008) 652–663.

[43] Hirschmuller, H. (2008). Stereo processing by semiglobal matching and mutual information. *IEEE Transactions on pattern analysis and machine intelligence*, *30*(2), 328-341.

[44] Dall'Asta, E., & Roncella, R. (2014). A Comparison of Semiglobal and Local Dense Matching Algorithms for Surface Reconstruction. International Archives of the Photogrammetry, Remote Sensing & Spatial Information Sciences, 45.

[45] ABAQUS/Standard User's Manual, Version 2018. Providence, RI: Simulia, 2018.